



# Random forest assisted vector displacement sensor based on a multicore fiber

JINGXIAN CUI,<sup>1,\*</sup> HUAIJIAN LUO,<sup>2</sup> JIANING LU,<sup>2</sup> XIN CHENG,<sup>1</sup> AND HWA-YAW TAM<sup>1</sup>

<sup>1</sup>Photonics Research Centre, Department of Electrical Engineering, The Hong Kong Polytechnic University, Hung Hom, Kowloon, Hong Kong, China

<sup>2</sup>Photonics Research Centre, Department of Electronic and Information Engineering, The Hong Kong Polytechnic University, Hung Hom, Kowloon, Hong Kong, China

\*jingxian.cui@connect.polyu.hk

**Abstract:** We proposed a two-dimensional vector displacement sensor with the capability of distinguishing the direction and amplitude of the displacement simultaneously, with improved performance assisted by random forest, a powerful machine learning algorithm. The sensor was designed based on a seven-core multi-core fiber inscribed with Bragg gratings, with a displacement direction range of 0–360° and the amplitude range related to the length of the sensor body. The displacement information was obtained under a random circumstance, where the performances with theoretical model and random forest model were studied. With the theoretical model, the sensor performed well over a shorter linear range (from 0 to 9 mm). Whereas the sensor assisted with random forest algorithm exhibits better performance in two aspects, a wider measurement range (from 0 to 45 mm) and a reduced measurement error of displacement. Mean absolute errors of direction and amplitude reconstruction were decreased by 60% and 98%, respectively. The proposed displacement sensor shows the possibility of machine learning methods to be applied in point-based optical systems for multi-parameter sensing.

© 2021 Optical Society of America under the terms of the [OSA Open Access Publishing Agreement](#)

## 1. Introduction

Displacement is one of the most important parameters in various industrial applications, including structural health monitoring [1], biomedical measurement [2], aerospace applications [3], etc. Numerous approaches have been proposed to measure one-dimension displacement of different amplitudes with high accuracies. However, developing a position tracking sensor in practical applications, such as robotic arms [4], two-dimensional sensing is needed. It requires the designed sensor to be sensitive to both the amplitude and direction of the applied displacement simultaneously. Several types of displacement sensors have been investigated based on different techniques such as mechanical [5], capacitive [6], electronic [7], and fiber-optic, etc. Among them, the fiber-optic displacement sensors have the edge over the others due to their intrinsic advantages, including electromagnetic interference immunity, miniature size, electrically-passive operation, and multiplexing capability [8–10]. Generally, fiber-optic displacement sensors are developed based on the measurement of deflection induced by fiber bending or stretching. Through monitoring the variation of intensity, wavelength and phase of the optical signal, the displacement performance is analyzed. In order to obtain the direction information of the displacement, several fiber-optic two-dimensional displacement sensors were reported, with the direction dependency resulted from an asymmetric geometry. For example, Yang et al. introduced a direction-dependent displacement sensor by inscribing gratings in the core and the inner cladding of a multi-cladding fiber [11]. Due to the intensity modulation difference between the two fiber Bragg gratings (FBGs), displacement induced output optical signal showed direction sensitivity. In addition, Bao et al. demonstrated a displacement sensor by inscribing an eccentric FBG in the core/cladding interface using a depressed-cladding fiber [12], which introduced a

cylindrical asymmetry into the fiber. The direction related displacement response was obtained through intensity detection. Although these sensors are displacement direction sensitive, the variation of displacement amplitude in a random direction is unknown. In other words, all the aforementioned sensors are not able to retrieve the displacement direction and amplitude simultaneously. Essentially, the displacement sensor response is caused by the displacement induced fiber bending. In order to retrieve the displacement information during the displacement measurement process, the relationship between the displacement and corresponding fiber bending is kept linear, which limits the measurement range within several micrometers (dependent on the length of the tested fiber). In addition, the reconstruction performance is mainly dependent on the accuracy of the corresponding theoretical model, where small variation may result in large error for each retrieval. Moreover, the system error is inevitable during the setup process, which may introduce larger error in each calculation process. To improve the displacement performance, an accurate method for the amplitude and direction reconstruction should be investigated.

Recently, different machine learning algorithms have been used to improve estimation accuracy in optical fiber sensors. For example, in distributed optical fiber sensing systems, researchers utilized algorithms such as support vector machine (SVM), principal component analysis (PCA), artificial neural networks (ANN), convolutional neural network (CNN), etc. to extract the Brillouin gain spectrum (BGS) [13–16], which was usually obtained using Lorentzian curve fitting (LCF) [16]. However, the accuracy of the extraction of BGS with the LCF approach is influenced by the fitting parameters. These machine learning algorithms enhance the sensing performance with an accurate and efficient BGS extraction, producing better performance over the conventional fitting method. In addition to the distributed optical fiber sensing, the point-based optical fiber sensing systems are also benefited from the machine learning tools. For instance, the Gaussian process regression (GPR) was introduced to an FBG-based temperature sensor for accurate temperature calculation [17]. It provided a direct mapping between the temperature and FBG spectrum to improve the detection accuracy, while conventional fitting methods were largely dependent on the quality of the FBG spectrum. In particular, there are researches using machine learning algorithms to distinguish multi-parameters in the point-based sensing systems, such as the discrimination of both the magnitude and location of applied normal force in an FBG-based tactile sensor using neural networks [18], and simultaneous measurement for amplitude and direction of the transverse load in a long-period grating (LPG)-based force sensor, where different regression algorithms were investigated for performance comparison [19]. In this work, we applied machine learning to the FBG-based vector displacement sensor for improvement on the measurement range and accuracy.

Various categories of machine learning algorithms are being applied to improve performance in optical sensors, such as neural networks and regression methods. Among them, random forest is regarded as one of the most precise prediction algorithms for classification and regression, due to its capability of modeling complex variable interactions [20]. It consists of a combination of tree predictors where each tree is generated using a random vector sampled independently from the input vector. Random forest algorithm has many advantages such as high efficiency for large dataset, insensitivity to noise or over-fitting, and fewer parameters when compared with other machine-learning algorithms (e.g., ANN or SVM). However, few studies have employed the random forest regression algorithm in fiber-optics sensing, especially for the vector displacement sensor. In this work, we demonstrated that the application of random forest algorithm can enhance the performance of vector displacement sensor substantially.

In this manuscript, we proposed a random forest assisted two-dimensional vector displacement sensor based on FBGs inscribed in a seven-core multi-core fiber (MCF), with the displacement direction range of 0–360°, and the amplitude range depends on the length of the sensor body. MCF has been proposed for various applications, including FBG-based curvature measurement [21], and the interferometer-based biomedical sensing [22,23]. Here, we proposed to use the

FBG-based MCF for a two-dimensional displacement measurement. The sensor can reconstruct the amplitude and direction of displacement simultaneously at any random position in the two-dimensional plane, and their performance using the theoretical model and the random forest algorithm are investigated. Due to the limitation of the theoretical model, the sensor was performed under a linear range (from 0 to 9 mm), while the measurement error was greatly dependent on the model quality and the system error. However, the random forest algorithm can help in both aspects, with an enhanced measurement range (from 0 to 45 mm) and a reduced measurement error for displacement. Mean absolute errors (MAEs) of direction and amplitude reconstruction were decreased by 60% and 98%, respectively. The application of random forest in the FBG-based displacement sensor shows the potential of the machine learning methods in improving the accuracy of point-based optical sensors, especially for scenario such as multi-parameter sensing.

## 2. Proposed displacement sensor

The seven-core MCF we used to develop the fiber-optic displacement sensor is fabricated by YOFC, China, with a central core in the middle and six outer cores arranged hexagonally around the central core. Figure 1(a) shows the schematic diagram of the cross-section of the MCF, with diameters for core  $D_0$  and cladding  $D$  of  $\sim 8$  and  $\sim 150 \mu\text{m}$ , respectively. The pitch  $d$ , the distance between two adjacent cores, is  $\sim 42 \mu\text{m}$ . In order to enhance the photosensitivity of the fiber, it was loaded in a hydrogen chamber for 3 days under a pressure of 100 bar at a temperature of  $\sim 80^\circ\text{C}$ . Then FBGs were inscribed using a 248 nm KrF excimer laser (Coherent) based on the phase mask (Ibsen Photonics, 1075.23 nm) and beam scanning technique. The FBGs were inscribed in all the seven cores simultaneously, with grating length of 10 mm and the scanning speed of 0.1 mm/s.

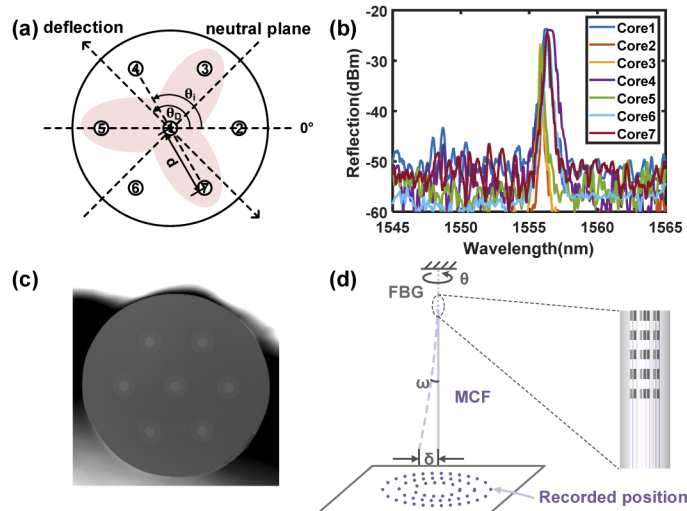


**Fig. 1.** (a) Geometrical definition of parameters based on the cross-section of the MCF. (b) Reflection spectra of FBGs inscribed in different cores at the same position. (c) Scanning electron microscopic figure of the seven-core MCF. (d) Schematic structure demonstration of the FBG and MCF in the displacement sensor design, with the schematic FBGs inscribed in MCF shown in the expanded view.

After the FBG inscription, the MCF was spliced to a 1-to-7 fan-out device (YOFC, China) using a polarization maintaining fiber fusion splicer (Fujikura, LZM-100). When the MCF in the fan-out device and the MCF probe are placed together at the two sides of the splicer, they

can be spliced through monitoring each of the end-view figure with the help of an “End View” program. The reflection spectra were recorded with an optical spectrum analyzer (YOKOGAWA, AQ6370D), as shown in Fig. 1(b). It is obvious that there is slight difference between the Bragg wavelength in each core, which is caused by the non-uniform UV exposure during the inscription process due to the spatial distribution of different cores [24,25]. Figure 1(c) shows the scanning electron microscope image of the MCF’s cross-section. During the displacement measurement, four of the seven cores, including the central one (i.e., core 1) and three outer ones (i.e., core 3, 5 and 7) are monitored.

### 3. Theoretical model of the displacement sensor

The applied displacement can be determined by measuring the Bragg wavelength shifts in different cores based on fiber displacement-induced bending. Due to the spatial distribution of the cores, some outer cores are compressed, which introduces a blue shift in the Bragg wavelength while the others are stretched and experienced a red shift. However, core 1 is insensitive to the applied displacement since it lies in the neutral plane, which can be utilized for temperature compensation [26,27]. As a result, the Bragg wavelength shift  $\Delta\lambda$  in a specific core  $i$  can be expressed as [25]

$$\Delta\lambda_i = (1 - p_e)\lambda_i \cdot \frac{d}{R} \cdot \sin(\theta_D + \theta_i), \quad (1)$$

where  $p_e$  representing the effective photo-elastic coefficient is  $\sim 0.22$  [28], and  $\lambda_i$  is the Bragg wavelength of core  $i$ . When displacement is applied to the MCF, the displacement angle is defined by  $\theta_D$  as shown in Fig. 1(a), where  $\theta_i$  indicates the corresponding angular position of each core  $i$  with respect to the  $0^\circ$  plane. In addition,  $R$  represents the displacement-induced bending radius. The designed sensor is based on a cantilever structure, as is shown in Fig. 1(d), with the displacement  $\delta$  applied on the free-fiber end and the other end kept fixed. The discrete points in Fig. 1(d) represent the recorded displacements, which are the projections of the free-fiber end with different directions and amplitudes. Based on the bending effect at a single FBG group at a short section along the fiber, and using the mechanical model between the displacement-induced bending radius and displacement amplitude, the displacement of an object on a plane can be monitored. The FBGs are located along the sensor body, with the structure shown in the expanded view. During measurement, the free-fiber end is shifted away from its origin position due to the applied displacement. As a result, the displacement-induced bending radius at a given position along the fiber length is defined as [29]

$$R(x) = \frac{EI}{M(x)} = \frac{EI}{-F(L-x)}, \quad (2)$$

where  $E$  and  $I$  are the Young’s modulus and the moment of inertia respectively, and  $M(x)$  indicates the bending moment at a specific position, which is related to the position  $x$ , free fiber length  $L$  and the applied force  $F$  at the free fiber end. Under this situation, the displacement  $\delta$  can be expressed by [29]

$$\delta = \frac{FL^3}{3EI}. \quad (3)$$

Based on Eqs. (2) and (3), we have the relationship between displacement and bending radius as follows

$$\delta = \frac{L^3}{3R(x)(x-L)}, \quad (4)$$

which indicates that the displacement is dependent on the free fiber length  $L$  and position  $x$ .

As a result, when Bragg wavelength shifts in two of the outer cores are considered, such as core  $i$  and  $j$ , the displacement angle  $\theta_D$  can be deduced by Eq. (5),

$$\theta_D = \tan^{-1} \left( \frac{\frac{\Delta\lambda_i}{\lambda_i} \sin \theta_j - \frac{\Delta\lambda_j}{\lambda_j} \sin \theta_i}{\frac{\Delta\lambda_j}{\lambda_j} \cos \theta_i - \frac{\Delta\lambda_i}{\lambda_i} \cos \theta_j} \right), \quad (5)$$

where the denominator should be non-zero, meaning the phase between  $\theta_i$  and  $\theta_j$  can be any value except  $\pi$ . In other words, core  $i$  and  $j$  should not be aligned in a straight line with the central one to determine the displacement direction. Once  $\theta_D$  is determined, the displacement amplitude is obtained via substituting Eq. (4) to Eq. (1), which can be expressed as

$$\delta = \frac{L^3}{3(1-p_e) \cdot \frac{\lambda_i}{\Delta\lambda} \cdot d \sin(\theta_D + \theta_i)(x-L)}. \quad (6)$$

Consequently, by measuring the Bragg wavelength shifts in different cores,  $\theta_D$  and  $\delta$  can be reconstructed from a random position, meaning that the proposed sensor has the capability of determining the direction and amplitude of the displacement simultaneously in the two-dimensional plane.

Based on Eq. (6), it is noticed that the theoretical model is effective based on a linear relationship between the wavelength shift and the displacement amplitude. However, the wavelength shifts would go into the nonlinear range when the applied displacement is too large, representing a limited measurement displacement amplitude range under this cantilever structure. Hence, in order to keep the linearity of the Bragg wavelength shift, the shifted angle  $\omega$  shown in Fig. 1(d) was limited to less than  $5^\circ$ , corresponding to a displacement amplitude range of 0 to 9 mm, which greatly compromised the sensor performance.

#### 4. Random forest model of the displacement sensor

Random forest regression is an ensemble machine learning algorithm [30]. It uses a large set of regression trees as base learners to constitute a forest for data training and predication [31]. Regression trees are run in parallel without interaction, where each of them grows on an individual bootstrap sample derived from the initial training data. Each node in a tree represents a binary test against the predictor variable. The variables at each node are selected to minimize the residual sum of squares of both branches.

To get an ensemble model with strong generalization, the regression tree in the model is set as uncorrelated as possible [30]. Random forest uses bagging [32], a parallel ensemble model to increase the diversity of trees. For an initial dataset with  $N$  samples, a bootstrap sample is created by randomly selecting  $N$  samples from the initial dataset with replacement (selected sample is returned to the initial dataset after one sampling, making it possible to be chosen during the next sampling). Prediction is constructed based on averaging the separate decisions from each tree in the forest. This characteristic makes random forest more robust when there is slight variation in input data, which enhances both the prediction accuracy and stability [32].

In this study, a Python-based random forest regression algorithm from the scikit-learn library was adopted for modelling. Since wavelength shifts of four of the seven cores were monitored during the measurement, a dataset constituting 8325 samples with four input variables was used. Two dependent variables, including the direction and amplitude of the displacement were correspondingly used as outputs. Flow chart of the random forest algorithm used for this sensor is illustrated in Fig. 2, with a tree number  $k$  of 100.

To ensure better fitting of the model, the input data was preprocessed. Ideally, the central core should always stay in the neutral plane during the measurement. However, there was an inevitable offset during the experiment. In addition, the central one was aimed for temperature

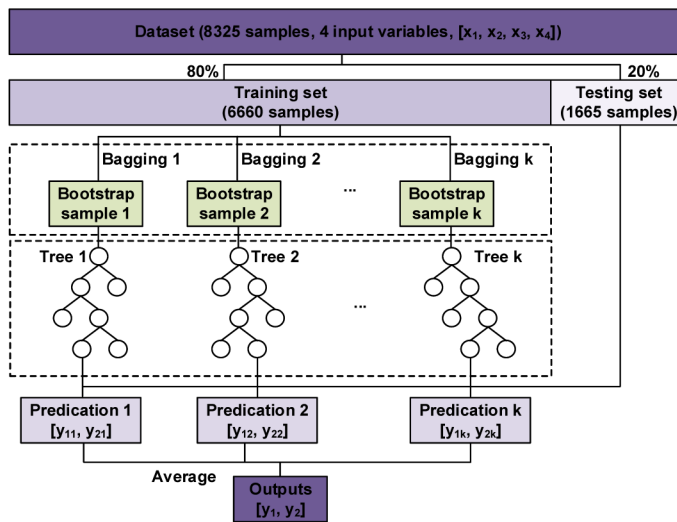


**Fig. 2.** Flow chart of random forest algorithm.

compensation, representing the information it carried independent from the other three. As a result, we subtracted the response of the central core from the rest of the input variables, meaning the sensor is still temperature-insensitive based on the random forest reconstruction. After preprocessing dataset, 80% of the dataset was randomly divided for training, while the left 20% was for testing.

## 5. Experimental setup and results

### 5.1. Experimental setup

Schematic of the experimental setup is illustrated in Fig. 3. The seven-core MCF inscribed with FBGs was mounted to a fiber rotator (Thorlabs, HFR007). Displacement was applied to the free end of the sensing fiber, and the other end was spliced to a 1-to-7 fan-out device. The MCF was clamped on the fiber rotator with the FBG-inscribed section free to bend. In order to interrogate the FBGs in different cores of the MCF, an interrogator (Micron Optics, sm130) with 1 pm resolution was connected to the single mode fibers (SMFs) of the fan-out device, such as core 1, 3, 5, and 7. Only the FBGs in four cores were measured, which was limited by our interrogator having four channels. Length of the free fiber was kept as 111 mm, with a displacement amplitude range of 0 to 45 mm, and the fiber rotator was used to change the direction within 360°. During the measurement, the displacement amplitude was varied by 1 mm and the direction was changed with a step of 10°.

### 5.2. Experimental results

During the experiment, FBG responses in core 1, 3, 5, and 7 were recorded, including a central core and three outer cores which were arranged in a regular triangle shape. Figures 4(a)–4(c) give the Bragg wavelength shift as a function of applied displacement amplitude for three outer cores under different directions in the linear range (1 to 9 mm in steps of 1 mm), with the dots in different shapes representing the experimental data, and the lines indicating the fitting curves (an average fitting  $R^2$  of 0.9995). The full range of the displacement amplitude was from 0 to 45 mm during the measurement, and the relationship became nonlinear with increasing amplitude. Therefore, the wavelength response of core 3 in the full range (1 to 45 mm in steps of 2 mm) is

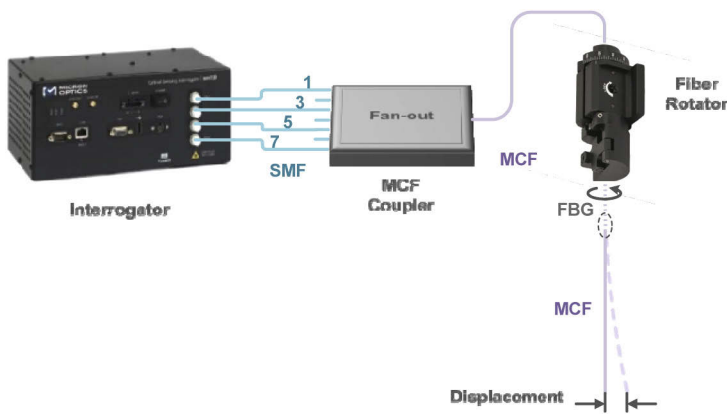


**Fig. 3.** Schematic experimental setup for the two-dimensional vector displacement sensor.

shown in Fig. 4(d) for demonstration, where dots represent the experimental results and lines are connecting curves. The theoretical model is no applicable for large displacement because the response become nonlinear.

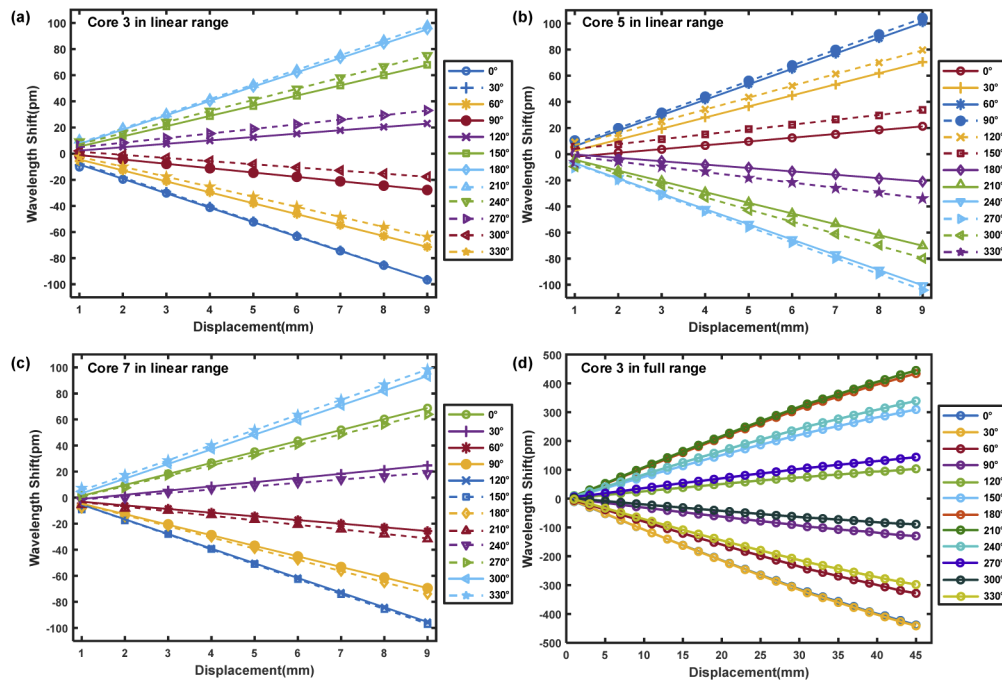


**Fig. 4.** Experimental results of wavelength shift versus displacement amplitude in linear range of (a) core 3, (b) core 5, (c) core 7, and wavelength response of (d) core 3 in full range. The displacement direction varies from 0 to 330° in steps of 30°, with the dots indicating the experimental results while the lines in (a)-(c) representing the fitting ones, and (d) representing the connecting curves.

In addition, the displacement sensitivities were recorded based on the slopes of the fitting lines in Figs. 4(a)–4(c), which were displayed in a polar coordinate as shown in Fig. 5. An ‘8’-shaped sensitivity response was observed, indicating a strong direction dependence. For a specific core,

such as core 3, the sensitivities are divided into the positive and negative parts, corresponding to the situation of stretching and compressing the FBGs during the measurement, respectively. The positive range for core 3 is recorded as  $110^\circ$ - $200^\circ$ - $290^\circ$ , while it is  $290^\circ$ - $20^\circ$ - $110^\circ$  for the negative sensitivity. Moreover, there is a  $120^\circ$  phase shift among the sensitivity response for individual cores, which is the same with their angular position difference as shown in Fig. 1(a). The maximum positive sensitivities are obtained as 11.47, 12.31, and 11.73 pm/mm for core 3, 5, and 7 individually, corresponding to the displacement directions of  $200^\circ$ ,  $80^\circ$ ,  $320^\circ$ . There is slight variation among the obtained sensitivity values, which is caused by the difference in the inscribed sensor depth during the fabrication process [21].

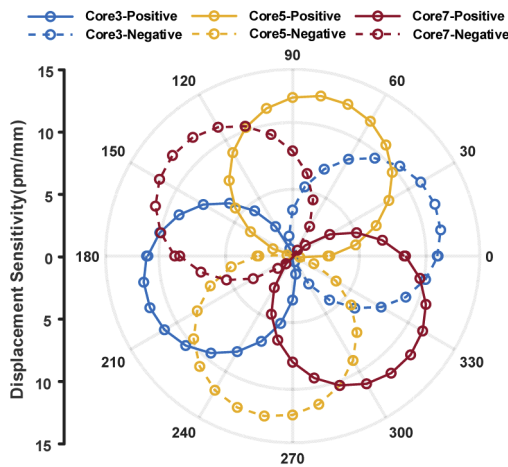


**Fig. 5.** Experimental results of sensitivity-direction response in core 3, 5 and 7, with displacement direction changing from 0 to  $360^\circ$  in steps of  $10^\circ$ .

## 6. Displacement retrieval

### 6.1. Retrieval performance with theoretical model

Equation (5) indicates that the displacement direction can be retrieved through monitoring the Bragg wavelength shifts in two of the outer cores, which are not aligned in a straight line with the central core, while the direction is independent on the displacement amplitude. In addition, due to the hexagonal structure of the arrangement for the seven-core MCF, there is one fiber core which locates at the central of the cladding, which can be utilized for the compensation of fiber mechanical offset and temperature change, as it is located in the neutral axis and thus is not affected by the fiber bending. Therefore, a combination of three cores is enough to reconstruct the displacement information based on the theoretical model. Here, two of the four outer cores are chosen, such as core 3 and core 5 (combination 1), core 3 and core 7 (combination 2), or core 5 and core 7 (combination 3), to retrieve the displacement direction, with the absolute error plotted in Fig. 6, which is defined as the absolute difference between the set direction and the measured one. Mean absolute errors (MAEs) of different combinations are  $3.23^\circ$ ,  $3.52^\circ$  and  $2.43^\circ$ , respectively. Based on Fig. 6, there are three characteristics of the direction error. First is the direction error found to be direction sensitive. A regular sinusoidal shape is observed in error maps, which is related to the sensitivity dependency of displacement direction, meaning there is a relatively smaller error under the direction with high sensitivity. Secondly, the error gets smaller when the displacement gets larger, which may be caused by the little variation under small displacement. Finally, there is a  $120^\circ$  phase shift between different combinations, which is matched with the sensitivity curve properly.

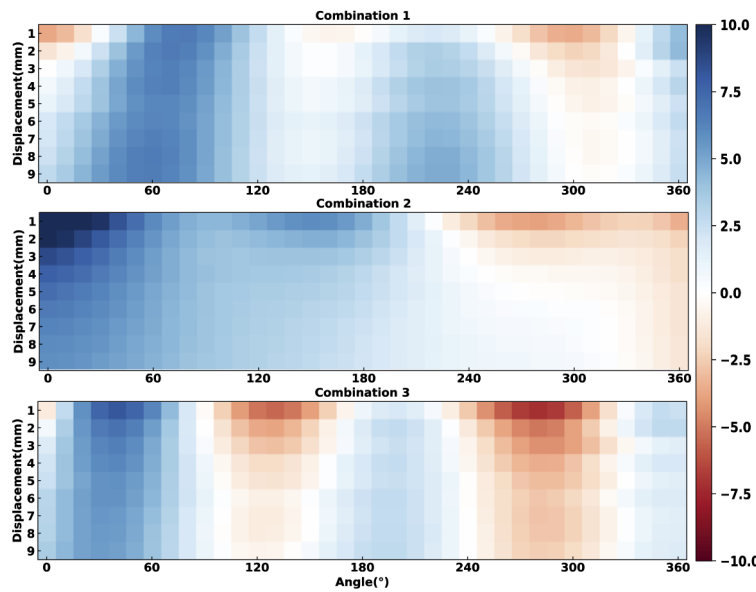


**Fig. 6.** Absolute errors of displacement direction based on different combinations of the outer cores using theoretical model, with the direction and displacement ranges of 0–360° and 1–9 mm, respectively.

After the determination of the displacement direction, the amplitude can be calculated with the help of Eq. (6). The displacement amplitude is obtained based on the combination of the reconstructed displacement direction and the angular position of one of the cores used in the direction calculation process. Hence, there are in total six combinations for the amplitude reconstruction. In addition, we only consider the linear range for reconstruction using the theoretical model. The displacement amplitude is set to change from 0 to 9 mm. Different from the direction, the amplitude is highly dependent on the value of the measured direction, meaning the errors introduced from the direction would have a negative impact on the reconstruction of the amplitude owing to the propagation of error. Figure 7 summarizes the displacement amplitude error based on different combinations, with each combination for direction calculation having two branches (a and b). MAEs are 12.67, 14.63, 9.7, 9.92, 11.58, and 8.29 mm for combination 1(a) to 3(b). Obviously, the errors are too large for meaningful retrieval. However, there is still a sinusoidal trend in the amplitude error map, where a small error happens under a high direction sensitivity with an interval of 180°, which is similar to the performance of the direction.

The poor performance of the amplitude retrieval based on the theoretical model could be caused by several factors, including the unprecise model, system error and the errors carried from the direction. In addition, the limited range is another disadvantage for the application of the displacement sensor. Overall, the retrieval performance based on the theoretical model greatly depends on the quality of the theoretical model, while little variation may cause large error during the retrieval process.

### 6.2. Improved performance with random forest regression

To assess the effectiveness of random forest regression, coefficient of determination  $R^2$  is used to evaluate the performance, which is defined as

$$R^2 = 1 - \frac{\sum (y_i - \hat{y}_i)^2}{\sum (y_i - \bar{y}_i)^2}, \quad (7)$$

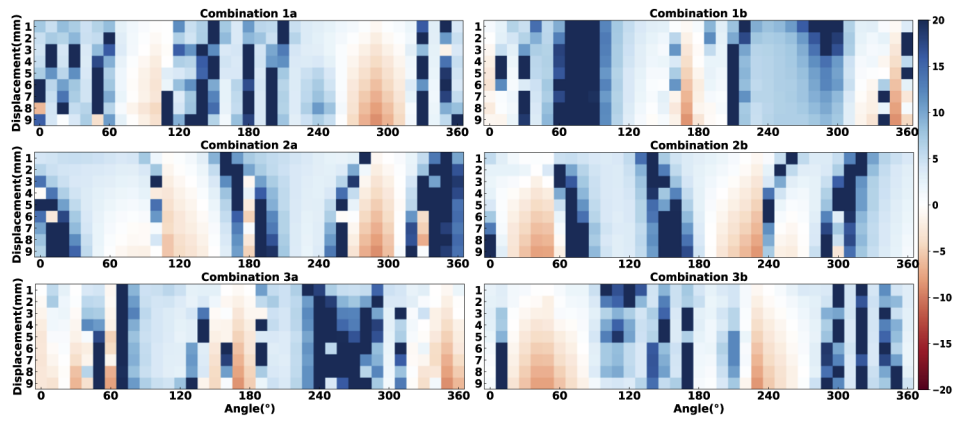


**Fig. 7.** Absolute errors of displacement amplitude based on different combinations of the outer cores using theoretical model, with the direction and displacement ranges of 0-360° and 1-9 mm, respectively.

where  $y_i$  and  $\hat{y}_i$  are the true and prediction value, and  $\bar{y}_i$  indicates the mean of label. The best score is 1.0, and we get a coefficient of 0.997, reflecting the good accuracy obtained with random forest algorithm. Similar to the evaluation of the theoretical model, the retrieval performance is also investigated for random forest, and the absolute error maps of the two parameters are shown in Fig. 8. Since the algorithm concerns only about the training data, the linearity is no longer a restriction during the retrieval process. The calculation range for amplitude is extended to 0-45 mm, while the direction range remains unchanged. MAEs of direction and amplitude are 1.22° and 0.14 mm, respectively.

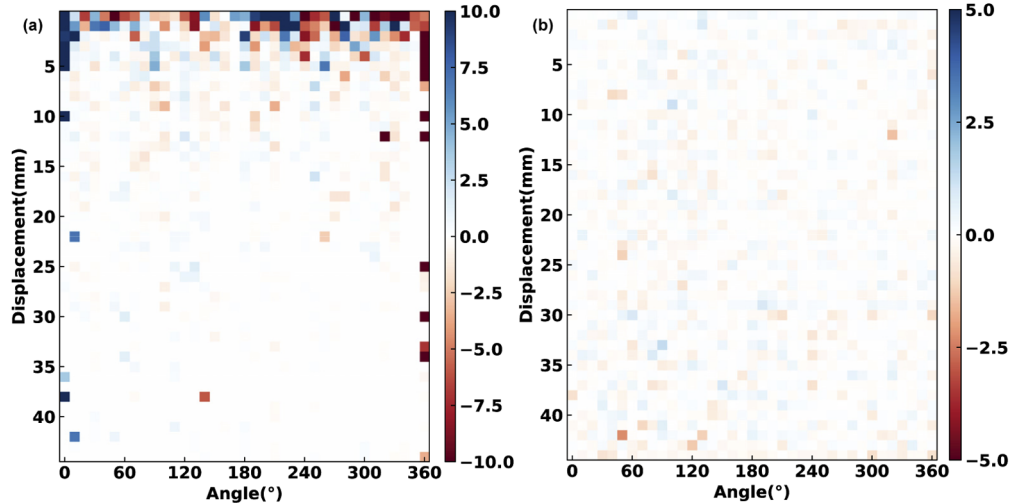


**Fig. 8.** Absolute errors of displacement (a) direction and (b) amplitude using random forest, with the direction and displacement ranges of 0-360° and 1-45 mm, respectively.

On the one hand, for the direction reconstruction, it is evident that the absolute error is smaller when increasing the displacement amplitude, which is similar to the performance of theoretical model. However, there remains no longer characteristic of direction sensitivity. With the increase of the amplitude, the direction retrieval becomes stable at most time, however it

becomes failure at very few points, which can be solved through enlarging size of the database. When comparing with the results obtained from theoretical model, the overall performance for the direction is enhanced by 60% with the random forest algorithm. On the other hand, there is a great enhancement in the retrieval of displacement amplitude, including the enlarged measurement range and decreased error. Since random forest predicts the amplitude based on averaging the predictions of trees, which is not a linear process compared to the theoretical model, where the linearity restriction disappears. As a result, the measurement range is enlarged by 5 times, which can be further enhanced through adjusting length of the fiber. In addition, the measurement error is reduced by 98% when comparing with the results from theoretical model, representing a perfect performance for the amplitude retrieval.

Furthermore, Table 1 summaries the comparison results of the reconstructed displacement information under two models, including the measurement range, and MAEs of displacement direction and amplitude.

**Table 1. Comparison between reconstructed results using two models**

Range	Theoretical model		Random forest model
	0-9 mm	0-45 mm	
MAEs of direction	Combination 1	3.23°	1.22°
	Combination 2	3.52°	
	Combination 3	2.43°	
	Average	3.06°	
MAEs of amplitude	Combination 1a	12.67 mm	0.14 mm
	Combination 1b	14.63 mm	
	Combination 2a	9.7 mm	
	Combination 2b	9.92 mm	
	Combination 3a	11.58 mm	
	Combination 3b	8.29 mm	
	Average	11.13 mm	

## 7. Conclusion

In summary, we have proposed a two-dimensional vector displacement sensor based on the FBGs inscribed in a seven-core MCF, with the capability of obtaining the displacement direction and amplitude simultaneously. The reconstruction performance was investigated under both the theoretical model and the random forest algorithm. We had a displacement direction ranged from 0 to 360°, while the measurable amplitude range related to the choice of the reconstruction method. For the performance based on theoretical model, the displacement amplitude range was dependent on the length of the fiber. It was performed under a linear range (from 0 to 9 mm). Meanwhile, the measurement error was greatly compromised by the model quality and the system error. However, the random forest model outperforms the theoretical model with an enhanced measurement range (from 0 to 45 mm) and a reduced measurement error for displacement. MAEs of direction and amplitude reconstruction were decreased by 60% and 98%, separately by using the random forest model. The application of random forest in the FBG-based two-dimensional displacement sensor enhanced the performance in both the accuracy and range. It also showed the potential for the machine learning methods to be applied in point-based optical sensing areas, especially for multi-parameter sensing.

**Funding.** Innovation and Technology Commission (BBVH); Research Grants Council, University Grants Committee (15210019).

**Disclosures.** The authors declare no conflicts of interest.

**Data availability.** No data were generated or analyzed in the presented research.

## References

1. H.-F. Pei, J. Teng, J.-H. Yin, and R. Chen, "A review of previous studies on the applications of optical fiber sensors in geotechnical health monitoring," *Measurement* **58**, 207–214 (2014).
2. H. A. Rahman, S. W. Harun, M. Yasin, and H. Ahmad, "Fiber-optic salinity sensor using fiber-optic displacement measurement with flat and concave mirror," *IEEE J. Sel. Top. Quantum Electron.* **18**(5), 1529–1533 (2012).
3. M. J. Nicolas, R. W. Sullivan, and W. L. Richards, "Large scale applications using FBG sensors: determination of in-flight loads and shape of a composite aircraft wing," *Aerospace* **3**(3), 18 (2016).
4. H. Xie, H. Liu, Y. Noh, J. Li, S. Wang, and K. Althoefer, "A fiber-optics-based body contact sensor for a flexible manipulator," *IEEE Sens. J.* **15**(6), 3543–3550 (2015).
5. F. Khoshnoud and C. W. d. Silva, "Recent advances in MEMS sensor technology-mechanical applications," *IEEE Instrum. Meas. Mag.* **15**(2), 14–24 (2012).
6. X. Liu, K. Peng, Z. Chen, H. Pu, and Z. Yu, "A new capacitive displacement sensor with nanometer accuracy and long range," *IEEE Sens. J.* **16**(8), 2306–2316 (2016).
7. M. R. Nabavi and S. N. Nihtianov, "Design strategies for eddy-current displacement sensor systems: review and recommendations," *IEEE Sens. J.* **12**(12), 3346–3355 (2012).
8. L. Qi, C.-L. Zhao, Y. Wang, J. Kang, Z. Zhang, and S. Jin, "Compact micro-displacement sensor with high sensitivity based on a long-period fiber grating with an air-cavity," *Opt. Express* **21**(3), 3193–3200 (2013).
9. J. N. Dash, R. Jha, J. Villatoro, and S. Dass, "Nano-displacement sensor based on photonic crystal fiber modal interferometer," *Opt. Lett.* **40**(4), 467–470 (2015).
10. P. Kisała, D. Harasim, and J. Mroczka, "Temperature-insensitive simultaneous rotation and displacement (bending) sensor based on tilted fiber Bragg grating," *Opt. Express* **24**(26), 29922–29929 (2016).
11. T. Yang, X. Qiao, Q. Rong, and W. Bao, "Orientation-Dependent Displacement Sensor Using an Inner Cladding Fiber Bragg Grating," *Sensors* **16**(9), 1473 (2016).
12. W. Bao, Q. Rong, F. Chen, and X. Qiao, "All-fiber 3D vector displacement (bending) sensor based on an eccentric FBG," *Opt. Express* **26**(7), 8619–8627 (2018).
13. H. Wu, L. Wang, N. Guo, C. Shu, and C. Lu, "Brillouin optical time-domain analyzer assisted by support vector machine for ultrafast temperature extraction," *J. Lightwave Technol.* **35**(19), 4159–4167 (2017).
14. A. K. Azad, F. N. Khan, W. H. Alarashi, N. Guo, A. P. T. Lau, and C. Lu, "Temperature extraction in Brillouin optical time-domain analysis sensors using principal component analysis based pattern recognition," *Opt. Express* **25**(14), 16534–16549 (2017).
15. A. K. Azad, L. Wang, N. Guo, H.-Y. Tam, and C. Lu, "Signal processing using artificial neural network for BOTDA sensor system," *Opt. Express* **24**(6), 6769–6782 (2016).
16. Y. Chang, H. Wu, C. Zhao, L. Shen, S. Fu, and M. Tang, "Distributed Brillouin frequency shift extraction via a convolutional neural network," *Photonics Res.* **8**(5), 690–697 (2020).
17. M. S. Djurhuus, S. Werzinger, B. Schmauss, A. T. Clausen, and D. Zibar, "Machine learning assisted fiber Bragg grating-based temperature sensing," *IEEE Photonics Tech. Lett.* **31**(12), 939–942 (2019).
18. L. Massari, E. Schena, C. Massaroni, P. Saccomandi, A. Menciassi, E. Sinibaldi, and C. M. Oddo, "A machine-learning-based approach to solve both contact location and force in soft material tactile sensors," *Soft Robot.* **7**(4), 409–420 (2020).
19. F. Barino, F. Delgado, M. A. Jucá, T. V. Coelho, and A. B. dos Santos, "Comparison of regression methods for transverse load sensor based on optical fiber long-period grating," *Measurement* **146**, 728–735 (2019).
20. X. Zhou, X. Zhu, Z. Dong, and W. Guo, "Estimation of biomass in wheat using random forest regression algorithm and remote sensing data," *Crop J.* **4**(3), 212–219 (2016).
21. M. Hou, K. Yang, J. He, X. Xu, S. Ju, K. Guo, and Y. Wang, "Two-dimensional vector bending sensor based on seven-core fiber Bragg gratings," *Opt. Express* **26**(18), 23770–23781 (2018).
22. R. Singh, S. Kumar, F.-Z. Liu, C. Shuang, B. Zhang, R. Jha, and B. K. Kaushik, "Etched multicore fiber sensor using copper oxide and gold nanoparticles decorated graphene oxide structure for cancer cells detection," *Biosens. Bioelectron.* **168**, 112557 (2020).
23. S. Kumar, G. Zhu, R. Singh, Q. Wang, B. Zhang, S. Cheng, F.-Z. Liu, C. Marques, B. K. Kaushik, and R. Jha, "MoS<sub>2</sub> Functionalized Multicore Fiber Probes for Selective Detection of Shigella Bacteria based on Localized Plasmon," *J. Lightwave Tech.* (2020).
24. E. Lindley, S.-S. Min, S. Leon-Saval, N. Cvetojevic, J. Lawrence, S. Ellis, and J. Bland-Hawthorn, "Demonstration of uniform multicore fiber Bragg gratings," *Opt. Express* **22**(25), 31575–31581 (2014).
25. J. Cui, Z. Liu, D. S. Gunawardena, Z. Zhao, and H.-Y. Tam, "Two-dimensional vector accelerometer based on Bragg gratings inscribed in a multi-core fiber," *Opt. Express* **27**(15), 20848–20856 (2019).
26. H. Zhang, Z. Wu, P. P. Shum, X. Shao, R. Wang, X. Q. Dinh, S. Fu, W. Tong, and M. Tang, "Directional torsion and temperature discrimination based on a multicore fiber with a helical structure," *Opt. Express* **26**(1), 544–551 (2018).
27. W. Hu, C. Li, S. Cheng, F. Mumtaz, C. Du, and M. Yang, "Etched multicore fiber Bragg gratings for refractive index sensing with temperature in-line compensation," *OSA Continuum* **3**(4), 1058–1067 (2020).

28. X. Dong, Y. Liu, Z. Liu, and X. Dong, "Simultaneous displacement and temperature measurement with cantilever-based fiber Bragg grating sensor," *Opt. Commun.* **192**(3-6), 213–217 (2001).
29. J. M. Gere, *Mechanics of Materials* (Bill Stenquist, 2004), Chap 9.
30. L. Breiman, "Random Forests," *Mach. Learn.* **45**(1), 5–32 (2001).
31. M. Kuhn and K. Johnson, *Applied predictive modeling* (Springer, 2013), Chap 19.
32. L. Breiman, "Bagging predictors," *Mach. Learn.* **24**(2), 123–140 (1996).